Journal of
Materials Chemistry A

ROYAL SOCIETY
OF CHEMISTRY

PAPER

View Article Online
View Journal | View Issue

Check for updates

Cite this: *J. Mater. Chem. A*, 2023, **11**, 8776

Defect-enrichment in porous interface of ultrathin CuO nanobelts realizes a novel CO_2 photoreduction pathway†

Qiang Wang,[a] Yanan Zhou,[b] Kaifu Zhang,*[ac] Yu Yu,[a] Qiquan Luo, *[d] Shan Gao *[a] and Yi Xie *[b]

Received 13th February 2023
Accepted 20th March 2023

DOI: 10.1039/d3ta00824j

rsc.li/materials-a

Selective photocatalytic conversion of CO_2 into liquid fuels *via* single component metal oxides represents an attractive strategy to achieve carbon balance and mitigate global warming. Herein, we for the first time propose that the integration of porous channel confinement and oxygen vacancy (V_O) for synergistically regulating the generation of key intermediates, enables highly selective CO_2 reduction and the controllable switches of specific CH_3OH or CO reaction pathways. *In situ* photoelectric characterization and theoretical calculations ensure that the versatile porous structure endows ultrathin CuO with an enrichment of catalytic sites coverage, improved adsorption microenvironment, and a short charge transport distance, assuring the excellent mass-transport and binding capability of reactants. This helps to facilitate inert CO_2 into a key reactive intermediate. Furthermore, the V_O near the porous interface, which is an actual catalytic site can regulate the formation energy of key intermediates for CO_2 activation, so that the adsorbed *CO can selectively generate a thermodynamically favorable *CHO intermediate with the corresponding Gibbs free energy change value being −0.09 eV (*vs.* 1.86 eV of perfect CuO), thus triggering a distinctive CH_3OH reaction pathway, rather than desorption, to release CO. Benefiting from these merits, the optimal CuO with a precise design enables the effective CO_2 photoreduction into value-added CH_3OH at an evolution rate of 12.3 μmol g^{-1} h^{-1}, a selectivity of 62.5%, and more importantly, a robust durability is realized, which is superior to most of the previously reported photocatalysts until now. This work sheds light on the fact that defect-enrichment in a porous interface can customize the unique reaction pathway for the CO_2 photoreduction to liquid fuels and offers a novel insight for the design of cheap and effective CO_2 photocatalysts.

1. Introduction

Photocatalytic reduction of CO_2 is a highly straightforward and appealing technology, for storing both inexhaustible light energy and excess CO_2 emissions in chemical bonds as value-added chemicals and fuels under mild conditions, which helps to achieve carbon neutralization and solve environmental issues in daily life.[1,2] However, among the key challenges in aiming for a massive application of artificial photosynthesis technology, is to control product selectivity due to the high C=O dissociation energy of inert CO_2 molecules, and the diversification of reaction routes. Among many CO_2 reduction reaction (CO_2RR) derivatives, methanol (CH_3OH) has more potential because of its high energy density, strong expandability and atomic economic value.[3] Specifically, CH_3OH, is a liquid product which is easy to store and transport, and can be widely used as a solvent and a raw material for basic chemical syntheses, pesticides and automobile fuel. It is worth noting that CH_3OH generation at the solid–liquid–gas interface was usually limited to the accessibility and mobility of surface species, where CO_2 and its rapid hydrogenation products are easy to attach to the catalyst surface, and which block the active sites, affecting the subsequent reaction.[4] In addition, due to uncontrollable changes in the adsorption energy and configuration of intermediates generated by multi-step proton coupled electron transfer during CO_2 reduction, as well as the low selectivity of CO_2 activation, a variety of products with similar reduction potential are competitively generated and dynamically transformed on the catalyst surface, which undoubtedly

---

[a] Anhui Province Key Laboratory of Chemistry for Inorganic/Organic Hybrid Functionalized Materials, Key Laboratory of Structure and Functional Regulation of Hybrid Materials of Ministry of Education, School of Chemistry and Chemical Engineering, Anhui University, Hefei, 230039, China. E-mail: shangao@ahu.edu.cn; kfzhang@ahu.edu.cn

[b] Hefei National Research Center for Physical Sciences at Microscale, University of Science & Technology of China, Hefei, 230026, China. E-mail: yxie@ustc.edu.cn

[c] Key Laboratory of Advanced Energy Materials Chemistry (Ministry of Education), Nankai University, Tianjin 300071, China

[d] Institutes of Physical Science and Information Technology, Anhui University, Hefei, 230039, China. E-mail: qluo@ustc.edu.cn

† Electronic supplementary information (ESI) available. See DOI: https://doi.org/10.1039/d3ta00824j

increases the cost of product separation. To enable the improved activity and selectivity of CO_2 conversion for CH_3OH production, developing cheap and efficient catalysts with unique structures to regulate the energy and adsorption configuration of active intermediate species on their surface is of great significance but it is still challenging.

To address the previous serious limitations, the objectives of high-efficiency catalyst design, include but are not limited to: (1) improve the mass transfer efficiency of obtained catalysts,[5] (2) increase the catalytically essential sites, and precisely manipulate the interaction between the active site and the reaction intermediate to customize the unique reaction pathway towards the desired CH_3OH generation during CO_2RR.[6,7] As such, many efforts have been made to construct catalysts for CO_2 photoreduction, with strategies such as nanostructure engineering,[8–10] heterostructures,[11–13] surface modification[14] and defect engineering[15–17] to tune their electronic structures and surface atomic arrangement for achieving a better CH_3OH yield and selectivity by improving the previous objectives. Among the materials used so far, copper-based materials are known as unique star series, which can convert CO_2 into liquid or value-added multicarbon (C_{2+}) compounds with impressive yield and efficiency.[18–20] As a consequence, we chose a popular copper oxide (CuO) semiconductor because of its low-cost, good conductivity, high abundance and excellent stability, which is expected to become a powerful substitute catalyst for CH_3OH photosynthesis to meet future energy industry needs.[21,22] More importantly, benefiting from its low valent $Cu^{\delta+}$ species (induced by the oxygen vacancies) with a relatively appropriate electron donor capacity, which can be used as an actual active site to combine with positively charged C atoms to confine specific intermediates and minimize their formation energy barrier of subsequent hydrides, to achieve selective CO_2 photoreduction matching the thermodynamic reduction potential of a desirable product.[23] A step further, the theoretical calculation results predicted that CuO with an optimized structure and intrinsic catalytic sites could better adsorb and activate CO_2.[24,25] Nevertheless, because of the low light utilization efficiency, improper energy band position, and poor product selectivity of CuO, the related research progress is rarely reported and remains unsatisfactory.

Inspired by the previous analysis and observations, it is desirable to urgently solve the challenge of material design for selective photocatalytic CO_2RR. Herein, we developed a porous CuO ultrathin nanobelt with a well-controlled oxygen vacancy (V_O) by using a wet chemical method combined with a fast calcination strategy. The diverse porous structure endows ultrathin CuO with an abundant coverage of catalytic sites, improved adsorption microenvironment for the binding capacity of CO_2, and a short charge transfer distance, ensuring excellent mass transfer and confinement of key reaction intermediates. More interestingly, the creation of V_Os diversifies the active sites and changes the local charge distribution of CuO, adjusting the interaction between reaction intermediates and active sites, which is conducive to the realization of highly selective CH_3OH production. As a consequence, combining these advantages, the catalysts obtained can selectively reduce CO_2 to CH_3OH with an evolution rate of 12.3 μmol g^{-1} h^{-1} after experiencing three cycles. Furthermore, the density functional theory (DFT) calculation and *operando* spectrochemistry technology reveal that the V_O near the porous interface as an actual catalytic site can regulate the formation energy of the key intermediates for CO_2 activation, so that the adsorbed *CO can selectively generate a thermodynamically favorable *CHO intermediate, thus triggering a distinctive CH_3OH reaction pathway, rather than desorption, to release CO. This work demonstrates the importance of defect-enrichment in a porous interface, in customizing the desirable product of CO_2 photoreduction, and this key catalyst design concept may be extended to other single-component 2D functional materials for a future CH_3OH economy.

2. Results and discussions

As a proof of concept, the gram-scale preparation of a porous CuO ultrathin series with controllable defects are developed using a novel two-step method to determine the effect of defect-enrichment in a porous interface in the photocatalytic activity of CO_2RR (Fig. S1, ESI†). As shown in Fig. 1a, the $Cu(OH)_2$ nanobelt was first prepared by using copper(II) chloride hydrate and sodium hydroxide as raw materials without any surfactant, and the $[Cu(OH)_4]^{2-}$ precursor self-assembly process was regulated by finely controlling the pH value of the mixture.[26] The X-ray diffraction (XRD) pattern of the product obtained showed that all the peaks belong to the monoclinic $Cu(OH)_2$ (PDF#80-0565), and the corresponding scanning electron microscope image

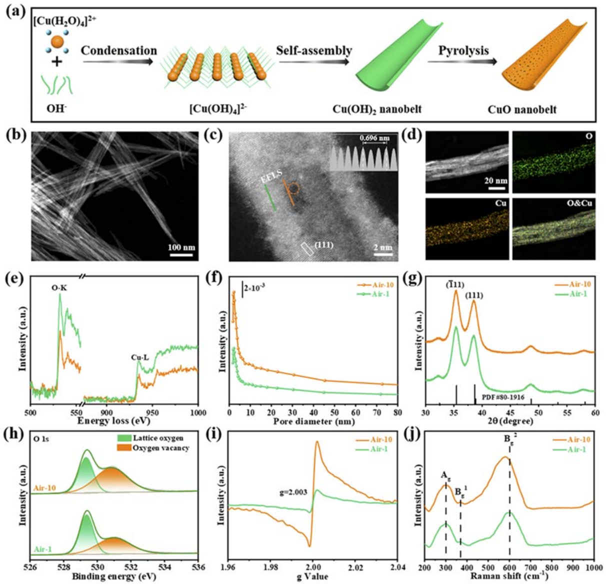

Fig. 1 (a) Schematic illustration of the synthetic process of a CuO nanobelt. (b) TEM image, (c) HAADF-STEM image (inset: intensity profiles recorded from the grey rectangular area), (d) EDX elemental mappings of air-10. (e) EELS spectra for the O-K and Cu-L edges (the solid orange and green lines are from the corresponding scan lines in (c)). (f) The pore-size distribution curves, (g) XRD patterns, (h) O 1s XPS spectra, (i) EPR spectra, and (j) Raman spectra of air-1 and air-10.

shows that it has a nanobelt-like structure, and a relatively smooth surface with lengths of ~2 μm and widths of ~20 nm (Fig. S2, ESI†). The ultrathin porous CuO nanobelts with an average thickness of 1.21 nm were successfully fabricated by fast-heating the precursors of the $Cu(OH)_2$ layers (Fig. S3, ESI†). The V_O level is modulated by accurately adjusting the annealing time in air. By calcining the precursor of ultrathin $Cu(OH)_2$ nanobelts at 250 °C in air for 10 min (denoted as air-10), an optimized porous CuO nanobelt rich in V_Os was obtained, and porous CuO with a different V_O content was prepared as a reference. To further reveal the fine structure of our constructed catalysts, the morphology and microstructure of air-10 and air-1 are characterized by transmission electron microscopy (TEM) and atomic-resolution high-angle annular dark-field scanning TEM (HAADF-STEM) (Fig. 1b–d and S4, ESI†), and the ultrathin belt-like structural features of them can be observed. The interplanar distances of 0.232 correspond to the (111) plane spacing of monoclinic CuO (PDF#80-1916) crystal. When compared with the air-1, air-10 has a rougher and porous surface, which is probably caused by volatile H_2O gas evaporation after a longer heat treatment. We demonstrated that the irregular black circles are actual nanopores because HAADF-STEM is a highly mass-sensitive imaging technique. Together with the micropores, a slight lattice disorder and dislocation (Fig. 1c) can be observed locally in the nanobelts, manifesting the existence of abundant point defects. Moreover, the low-loss electron energy loss spectroscopy (EELS) shows that the peak intensity of the O K-edge in air-10 is remarkably lower than that from the air-1 sample, thus, corroborating the irreversible loss of O during calcination, which contributes to formation of V_Os and nanopores (Fig. 1e).[27–29] This is in accordance with the corresponding energy-dispersive X-ray spectroscopy (EDS) elemental mapping results, the molar fraction of uniformly distributed Cu and O elements in air-10 is determined to be ~0.959 : 1 (Fig. 1d and S5, ESI†), further confirming the existence of V_Os. More importantly, the nanopores have a similar composition as the surrounding material. Additional evidence can be found in their pore size distribution curve shown in Fig. 1f, and micropores with a mean size of ~2 nm are displayed for air-10 and air-1. It is well known that there are many coordination unsaturated defect sites distributed around the pore, which favor the selective adsorption and enrichment of gas molecules and other reactive species on the surface of the photocatalyst during CO_2RR. Consequently, to confirm the existence of defects and investigate their properties further, a series of advanced analytical tools were employed to characterize the defect-controlled nanobelts. From Fig. 1g, all the diffraction peaks of air-1 and air-10 are well matched well with the diffraction data of monoclinic CuO, which is consistent with the TEM result. We further checked the results by X-ray photoelectron spectroscopy (XPS) and electron paramagnetic resonance (EPR) and so on. The fitting peaks of O 1s at 529.4 and 531.1 eV correspond to the lattice oxygen and the surface hydroxyl adsorbed at V_O, respectively (Fig. 1h), which indicated the existence of V_O. This also affects the valence state of Cu, leading to the formation of low-valent Cu^+ species in the CuO lattice confirmed by the Cu 2p XPS results (Fig. S6, ESI†).[30] In sharp contrast to air-1, the peak area of the oxygen atoms in the vicinity of V_O in air-10 at 531.1 eV is much stronger, indicating the presence of more oxygen defects. The EPR spectra were further recorded to identify the V_O. The typical EPR signal at $g =$ 2.003 for air-1 and air-10 is shown in Fig. 1i, which can be identified as the electrons captured in the V_Os.[31,32] Notably, the higher EPR signal of air-10 than that of air-1 confirms the richer V_O species formed, which also agrees well with the XPS results. In addition, the Raman bands of air-10 with abundant defective V_O species present, peak broadening and a blueshift relative to the air-1, which may be assigned to phonon softening or improved electron–phonon coupling at the V_O sites (Fig. 1j).[33] All of the analyses verify that V_Os and a porous structure have been successfully introduced onto the surface of air-10.

The unique nanobelt structure provides high porosity and enrichment of defective sites on the catalyst surface, which can offer a promising platform to unveil the influence of O defects and porous structures on mass transfer in CO_2RR. The photocatalytic CO_2RR activities of the catalysts obtained without any sacrificial agents were evaluated and analyzed by gas chromatography (GC) and ^{1}H-nuclear magnetic resonance spectroscopy (^{1}H-NMR) (Fig. S7 and S8, ESI†). As shown in Fig. 2a, S9 and S10 (ESI†), the main products of air-1 are CO and H_2, whereas the predominant products of other catalysts are CH_3OH accompanied by a small amount of CH_4. Notably, the air-10 achieved the highest CH_3OH evolution rate of 12.3 μmol g^{-1} h^{-1} and the CH_3OH selectivity reached nearly 62.5%, which was quite competitive with some other Cu-based materials and many previously reported state-of-the-art photocatalysts tested under comparable reaction conditions (Table S1, ESI†). In addition, the as-prepared air-10 sample could simultaneously realize H_2O oxidation into O_2 and CO_2RR with increasing irradiation time (Fig. S10, ESI†). What is more interesting, is that the yield and selectivity of CH_3OH on air-10 exhibit a positive correlation with the V_O density, suggesting that the suitable V_O are likely to be the actual active sites for the CO_2RR (Fig. S11 and Table S2,

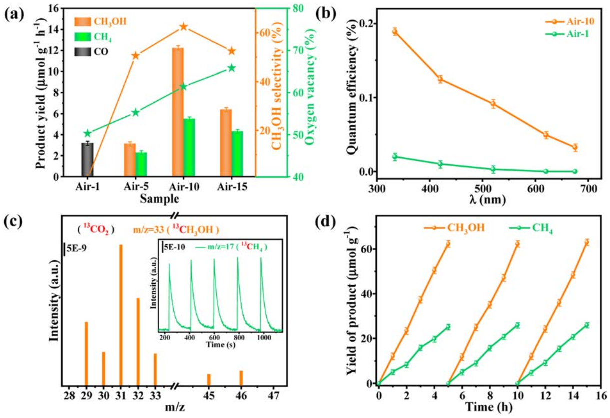

Fig. 2 (a) Product yields, CH_3OH selectivity and oxygen vacancy content of different photocatalysts. (b) QE values of air-1 and air-10, respectively. (c) GC-MS spectra of $^{13}CH_3OH$ and $^{13}CH_4$ generated from $^{13}CO_2$ photoreduction of air-10. (d) Photocatalytic stability of air-10.

ESI†). It is worth noting that the oxygen vacancies in air-15 can significantly improve the light utilization efficiency, whereas the excessive defect sites can also act as photogenerated carrier recombination centers to block the reaction, causing its decreased catalytic activity.[34,35] To further verify the photocatalytic activity, we conducted the quantum efficiency (QE) measurement in the range of 334–675 nm (Fig. S12, ESI†). As shown in Fig. 2b, the apparent QE of air-10 is determined to be 0.19% at 334 nm, which is consistent with the increased photocatalytic performance shown in Fig. 2a. In addition, a $^{13}CO_2$ isotopic labeling experiment was employed to track the carbon source in the reaction (Fig. 2c), and the significant peaks with *m*/*z* of 33 and 17, corresponded to $^{13}CH_3OH$ and $^{13}CH_4$, respectively, when $^{13}CO_2$ was used as the gas source, which verified that the evolved products were indeed derived from CO_2 photoreduction. As revealed by the control experiments, there was no detectable product generation in the dark, under Ar or in the absence of catalysts, which further supported the results of the $^{13}CO_2$-labelling experiments (Fig. S13, ESI†). More importantly, the air-10 did not show any obvious decline after three cycles up to a total of 15 h of photocatalysis (Fig. 2d). In this regard, XPS, EPR, XRD and STEM measurements of the used air-10 show no obvious structure and morphology variation relative to the fresh one, which provides crucial evidence for their excellent photostability (Fig. S14, ESI†).

To unravel the underlying reasons for the improved performance of the CO_2 photoreduction, several photoelectrochemical characterizations were employed. As shown in Fig. 3a, the air-10 shows a stronger absorption range from visible light to infrared light, and a red-shifted edge relative to the air-1, demonstrating the superior light harvesting capability for photocatalytic reactions, which may be the presence of the V_O resulting in the generation of several new intermediate energy levels thereby optimizing the band gap structure. In addition, the band structures of air-10 and air-1 were found to be 1.35 and 1.50 eV, respectively, by using the Kubelka–Munk function. The valence band (VB) positions of air-10 and air-1 are 0.87 and 0.90 V (*vs.* NHE), and the conduction band (CB) potentials of air-10 and air-1 are −0.48 and −0.60 V, respectively, suggesting that they are thermodynamically feasible for simultaneous CO_2 reduction and an H_2O oxidation reaction (Fig. 3b and c). Noticeably, the CB minimum of air-10 is slight lower than the reduction potentials of the CO_2/CO couples, which corresponds to its excellent photocatalytic CH_3OH yield and selectivity during CO_2 photoreduction. This is further supported by the result of the transient photocurrent measurement. The higher transient photocurrent response of air-10 indicating an enhancement in charge generation and separation in comparison to the other counterpart (Fig. 3e). The carrier density was determined using the Mott–Schottky measurements. Both samples exhibit similar negative slopes, as expected for the p-type nature of the CuO semiconductor. Air-10 has a smaller slope in contrast to air-1, which suggests that significantly improved donor densities are estimated by the following equations:

$$N_d = (2/e_0\varepsilon_r\varepsilon_0)[d(1/C^2)/dE]^{-1} \quad (1)$$

where e_0 (1.602×10^{-19} C), ε_r (25 for CuO), ε_0 (8.85×10^{-14} F cm^{-1}) and N_d are the electron charge, dielectric constant, vacuum permittivity, and carrier density of the photocatalysts, respectively.[36] Moreover, the N_d was calculated to be 7.8×10^{21} cm^{-3}, approximately 1.23 times higher than the 6.32×10^{21} cm^{-3} for air-1, thus this facilitates charge transfer and migration at the V_O sites. In the meantime, air-10 shows a smaller electrochemical impedance spectroscopy (EIS) radius and a weaker steady-state photoluminescence (PL) intensity than those of air-1, reaffirming that the high overall conductivity effectively realizes a faster interface charge transmission, and lower charge recombination rate (Fig. 3d and f). In addition, the transient-state PL (TSPL) spectroscopy is an effective tool and was employed to investigate the charge dynamics of the photogenerated charge carriers. The curves of both materials could be fitted by the tri-exponential decay model and the corresponding data are listed in Table S3 (ESI†). The average PL lifetime (τ_{ave}) of air-10 is obviously longer when compared to air-1. This means that the localized polarization effect induced by richer V_O sites promotes the defect states in the band gap to trap longer lived electrons, which is conducive to the subsequent interfacial CO_2RR process.[37] Therefore, the previous experimental results together show that the V_O sites ameliorates the light absorption and charge carrier separation of the air-10, and achieves greatly enhanced photocatalytic activities in CO_2RR.

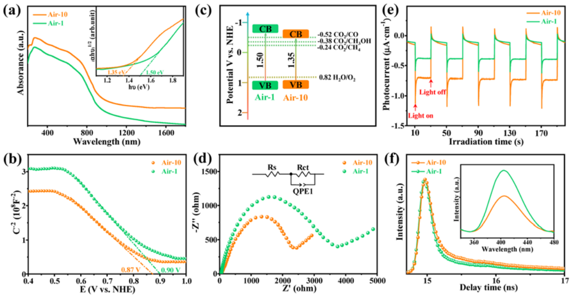

Fig. 3 (a) The UV-vis absorption spectra (inset: Tauc plots), (b) the Mott–Schottky plots, (c) the energy band structure alignments, (d) the EIS spectra, (e) the transient photocurrent responses (0.33 V *vs.* Ag/AgCl, pH = 7), (f) the TSPL decay (inset: steady-state PL spectra) of air-1 and air-10, respectively.

The surface reactant and reaction intermediate adsorption is generally considered as another prerequisite for the interfacial photocatalysis process. Of note, the creation of a porous structure on the air-10 surface dramatically boosts its surface area (109.13 m^2 g^{-1}), which will endow air-10 with an improved adsorption microenvironment, and a short charge transport distance, thus promoting the selective conversion of reactants at active defect sites (Fig. S15, ESI†). As shown by the Bader charge analysis in Fig. 4a and b, air-10 has more V_Os than air-1, and the spatial charge distribution nearby the V_Os becomes more delocalized, and negative charged due to the overlap of their electronic orbitals, which is conducive to adsorbing more CO_2 on its surface. As expected, the CO_2 adsorption isotherm shown in Fig. 4c further verifies this deduction, and air-10 has

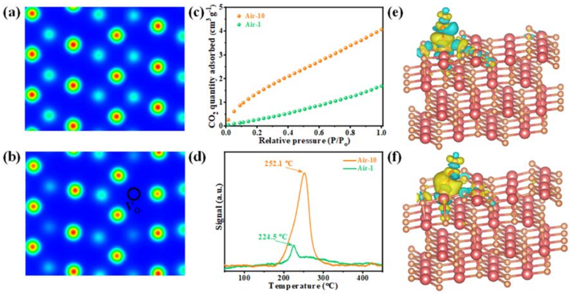

Fig. 4 Distribution of charge density for (a) perfect-CuO, and (b) V_O-CuO plotted from 0 (blue) to 2.6 e^- $bohr^{-3}$ (red). (c) The CO_2 adsorption isotherms, (d) the CO_2-TPD spectra of air-1 and air-10. Charge difference diagrams of *CO adsorption on (e) perfect-CuO and (f) V_O-CuO, yellow and blue spheres represent charge accumulation and depletion, respectively.

a higher CO_2 adsorption capacity. Furthermore, CO_2 temperature-programmed desorption (TPD) measurements were performed and the results are presented in Fig. 4d. In sharp contrast to air-1, it can be clearly observed that the chemisorption peak of air-10 shifts to a higher temperature (~252.1 °C), which proves that the chemical affinity of CO_2 on the surface V_O sites is remarkably strong.[38] This significant enhancement of CO_2 chemisorption may provide more opportunities to accelerate the activation of CO_2 into highly active intermediates to achieve efficient CH_3OH synthesis. In general, the engineered V_O can adjust the surface atomic configuration of the catalyst, thereby affecting the coordination mode and the activation energy barrier of the intermediate at the actual catalytic site on the catalyst surface, which is the key factor to determining product selectivity. Interestingly, the evolution of the *CO intermediate adsorbed on the V_O tuning surface is endothermic or exothermic, and controls the formation of multi-electron CO_2 reduction products. As such, the differential charge density calculation was employed to track the electron transfer between the CuO and *CO intermediates.[39] In this case, the formation and accumulation of the *CO intermediate on two models including a CuO surface with one V_O and a perfect CuO surface have been constructed and taken into consideration (Fig. 4e and f). As for a defective surface, the coordinately unsaturated Cu atoms neighboring the V_O sites inject their workable d-orbital electrons into the σ C–O antibonding orbital (σ*) and decrease the C–O bond strength. According to the calculation, the C–O bond in the *CO intermediate is elongated from 0.1146 to 0.1152 nm after the introduction of the suitable V_O species. Because of their bond distance difference, the *CO intermediate can easily generate the lower-energy *CHO intermediate by its own rapid protonation during the CO_2 photoreduction. This is also in agreement with the observation of the CO-TPD experiments over the CuO catalysts (Fig. S16, ESI†). Compared with air-1, the obvious chemical desorption peak of air-10 moving towards a higher temperature, indicating that air-10 shows a higher chemical bonding ability for the CO molecules. As predicted, this strong adsorption capacity can undoubtedly promote the subsequent hydrogenation reaction of the CO species. In addition, we also performed a CO photocatalytic performance test under similar conditions to support the proposed mechanism (Fig. S17, ESI†). We found that air-10 shows an excellent catalytic activity and CH_3OH selectivity, whereas air-1 has no activity. Taken together, these results prove that defect-enrichment in the porous interface of ultrathin CuO nanobelts can accelerate the hydrogenation of *CO species to form a *CHO intermediate, thereby altering the reaction pathway to form CH_3OH rather than desorbing it from its surface to generate CO molecules.

To obtain solid evidence, the *CHO species was probed by *in situ* Fourier-transform infrared spectroscopy (FT-IR) spectra using the air-10 catalyst. In comparison to air-1 with a smaller V_O, the infrared peaks at 1092, 1216, 1368, and 1478 cm^{-1} can be assigned to the *CHO, *OCH_3, *CH_3, and *OCH_2 species stretching mode of CH_3OH adsorbed on the surface of ultrathin air-10 nanobelts, of which the concentration of the active species are stronger with increasing irradiation time, which is consistent with the results from most of the previous reports (Fig. 5a and b).[40–43] While, it was found that no characteristic intermediate was present except for *COOH the intermediate generation on air-1 in the CO_2RR process, of which the *COOH intermediate is usually considered as a rate-determining step for CO_2 photoreduction, which is in good agreement with its above superior CO_2-to-CO photocatalytic activity.[44] Both

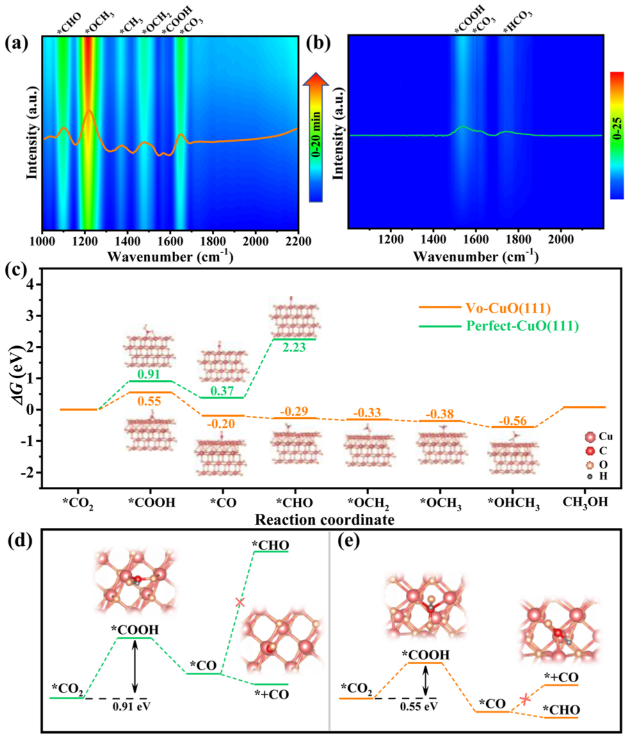

Fig. 5 *In situ* FT-IR spectra of (a) air-10 and (b) air-1. The inside solid orange and green lines were *in situ* FT-IR spectra of air-10 and air-1 under 20 min illumination, respectively. (c) Free energy diagrams for reduction of CO_2 over perfect-CuO and V_O-CuO based on DFT calculation as well as the corresponding structure models for each reaction step. Key steps of CO_2 photoreduction over (d) perfect-CuO and (e) V_O-CuO.

experimental and computational results verify that the CO_2 is more conducive to photocatalytic conversion into *CHO species on the surface of air-10. Recently, it has been reported that *CHO is a crucial intermediate in typical CO_2-to-CH_3OH reactions. Thus, we speculate that the most likely reaction pathways for this CO_2RR system are:

$$\mathrm{CO_2(g)} \rightarrow {}^{*}_{1}\mathrm{CO_2} \tag{2}$$

$$\mathrm{H_2O} \rightarrow \mathrm{H^+} + \mathrm{OH^-} \tag{3}$$

$${}^{*}_{1}\mathrm{CO_2} + \mathrm{H^+} + \mathrm{e^-} \rightarrow {}^{*}_{1}\mathrm{COOH} \tag{4}$$

$${}^{*}_{1}\mathrm{COOH} + \mathrm{H^+} + \mathrm{e^-} \rightarrow {}^{*}_{1}\mathrm{CO} + \mathrm{H_2O} \tag{5}$$

$${}^{*}_{1}\mathrm{CO} + \mathrm{H^+} + \mathrm{e^-} \rightarrow {}^{*}_{1}\mathrm{CHO} \tag{6}$$

$${}^{*}_{1}\mathrm{CHO} + \mathrm{H^+} + \mathrm{e^-} \rightarrow {}^{*}_{1}\mathrm{OCH_2} \tag{7}$$

$${}^{*}_{1}\mathrm{OCH_2} + \mathrm{H^+} + \mathrm{e^-} \rightarrow {}^{*}_{1}\mathrm{OCH_3} \tag{8}$$

$${}^{*}_{1}\mathrm{OCH_3} + \mathrm{H^+} + \mathrm{e^-} \rightarrow {}^{*}_{1}\mathrm{OHCH_3} \tag{9}$$

where * represents the surface adsorption state.

To test the deduction, further DFT calculations were adopted to predict the CO_2 conversion process based on two different structural models, the perfect CuO and V_O-CuO with a (111) exposed surface, respectively. As displayed by the stepwise Gibbs free energy profiles and the corresponding reactive intermediates' configuration (Fig. 5c), the formation of *COOH on V_O-CuO with a reaction free-energy difference of 0.55 eV by the first proton-coupled electron transfer step is much lower than that on the perfect CuO (0.91 eV). This decreased energy demonstrates that the introduction of the charge-enriched V_O sites can effectively stabilize the *COOH intermediate and facilitate the dynamic electron-transfer for the subsequent reaction, thereby leading to the improved photocatalytic performance of V_O-CuO compared with that of perfect CuO. Most interestingly, the Gibbs free energy of V_O-CuO for forming *CHO is significantly less than the CO desorption energy, and the generation of the *CHO radical is exothermic, whereas the desorption of *CO is endothermic and requires a greater energy input (Fig. 5d and e), which means that the introduction of Vo is more conducive to *CO protonation to generate CHO* instead of desorption to release CO. Conversely, the *CO desorption is exothermic whereas *CO protonation is highly endothermic, implying that the *CO molecules can be more easily desorbed from perfect CuO to evolve free CO molecules rather than its subsequent high-energy hydrogenation. In other words, the V_O-regulated porous surface effectively stabilizes and confines the adsorbed *CHO intermediates by greatly changing the endoergic protonation process of *CO, thereby realizing the preferred lower-energy CH_3OH reaction pathway, which is consistent with the previously mentioned theoretical scenario and experimental observations of the air-10 assign the dramatically favored selective photocatalytic CO_2 reduction to CH_3OH.

3. Conclusions

In summary, we demonstrate that a porous CuO ultrathin nanobelt catalyst prepared *via* a wet chemical method in conjunction with rapid calcination strategy, selectively photoreduces the CO_2 to CH_3OH, and clarifies the source of its excellent CO_2RR activity. In particular, the abundant porous structure on the surface of the nanobelts promotes the mass transfer of reactants and shortens the migration distance of photogenerated carriers. More importantly, numerous coordinatively unsaturated sites around the pore are rich in delocalized electrons, which can accelerate the polarization of the adsorbed reactants, thus producing active intermediates with optimized energy, and achieving selective customization of the target products. These synergistic merits endow the air-10 catalyst with a remarkably improved yield of CH_3OH as well as high stability, which is superior to the other counterparts produced under comparable conditions. This work paves the way for the design of high-performance catalysts, and provides in-depth insights into the kinetics and mechanism of the practical application of artificial photosynthesis.

Author contributions

YX and SG conceived and designed the research. QW carried out the experiments. QQL and YNZ carried out the DFT calculations. KFZ and YY participated in the experimental data analyses and scientific discussions. SG and KFZ wrote the manuscript. QW and YNZ contributed equally to this work.

Conflicts of interest

There are no conflicts to declare.

Acknowledgements

The work was supported by the National Natural Science Foundation of China (Grant No. U1832189, U21A20317, 22288201, 22102167 and 22205002), the research start-up fund from Anhui University (Grant No. S020118002/060 and S020318008/016) and the University Synergy Innovation Program of Anhui Province (Grant No. GXXT-2020-001). The calculations were performed on the Supercomputer of Anhui University and the National Supercomputing Center in Shanghai.

References

1 J. Xu, H. Xu, A. Dong, H. Zhang, Y. Zhou, H. Dong, B. Tang, Y. Liu, L. Zhang, X. Liu, J. Luo, L. Bie, S. Dai, Y. Wang, X. Sun and Y. Li, *Adv. Mater.*, 2022, **34**, 2206991.
2 Y. Wang, Y. Qu, B. Qu, L. Bai, Y. Liu, Z. Yang, W. Zhang, L. Jing and H. Fu, *Adv. Mater.*, 2021, **33**, 2105482.
3 L. Xiao, X. Li, Y. Jia, G. Hu, J. Hu, B. Yuan, Y. Yu and G. Zou, *Nat. Commun.*, 2021, **12**, 318.
4 Z. Liu, Y. Du, R. Yu, M. Zheng, R. Hu, J. Wu, Y. Xia, Z. Zhuang and D. Wang, *Angew. Chem., Int. Ed.*, 2023, **62**, e202212653.

5 Y. Xin, Y. Huang, K. Liu, Y. Yu and B. Zhang, *Sci. Bull.*, 2018, **63**, 601–608.

6 G. Zhang, T. Wang, M. Zhang, L. Li, D. Cheng, S. Zhen, Y. Wang, J. Qin, Z. Zhao and J. Gong, *Nat. Commun.*, 2022, **13**, 7768.

7 Z. Jiang, X. Xu, Y. Ma, H. Cho, D. Ding, C. Wang, J. Wu, P. Oleynikov, M. Jia, J. Cheng, Y. Zhou, O. Terasaki, T. Peng, L. Zan and H. Deng, *Nat*, 2020, **586**, 549–554.

8 X. Zhang, X. Wang, W. Wu, X. Chen and Z. Wu, *J. Mater. Chem. A*, 2019, **7**, 6963–6971.

9 H. Mistry, A. Varela, S. Kühl, P. Strasser and B. Cuenya, *Nat. Rev. Mater.*, 2016, **1**, 1–14.

10 Y. Li, Y. Sun, Y. Qin, W. Zhang, L. Wang, M. Luo, H. Yang and S. Guo, *Adv. Energy Mater.*, 2020, **10**, 1903120.

11 C. Bie, B. Zhu, F. Xu, L. Zhang and J. Yu, *Adv. Mater.*, 2019, **31**, e1902868.

12 J. Hao, Z. Zhuang, K. Cao, C. Wang, F. Lai, S. Lu, P. Ma, W. Dong and T. Liu, *Nat. Commun.*, 2022, **13**, 2662.

13 D. Deng, K. Novoselov, Q. Fu, N. Zheng, Z. Tian and X. Bao, *Nat. Nanotechnol.*, 2016, **11**, 218–230.

14 H. Luo, B. Li, J. Ma and P. Cheng, *Angew. Chem., Int. Ed.*, 2022, **61**, e202116736.

15 J. Wu, X. Li, W. Shi, P. Ling, Y. Sun, X. Jiao, S. Gao, L. Liang, J. Xu, W. Yan, C. Wang and Y. Xie, *Angew. Chem., Int. Ed.*, 2018, **130**, 8855–8859.

16 D. Yan, Y. Li, J. Huo, R. Chen, L. Dai and S. Wang, *Adv. Mater.*, 2017, **29**, 1606459.

17 Y. Zhang, L. Tao, C. Xie, D. Wang, Y. Zou, R. Chen, Y. Wang, C. Jia and S. Wang, *Adv. Mater.*, 2020, **32**, 1905923.

18 D. Yang, S. Sarina, H. Zhu, H. Liu, Z. Zheng, M. Xie, S. Smith and S. Komarneni, *Angew. Chem., Int. Ed.*, 2011, **50**, 10594–10598.

19 S. Bai, H. Qiu, M. Song, G. He, F. Wang and L. Guo, *eScience*, 2022, **2**, 428–437.

20 H. Zhang, C. Xu, X. Zhan, Y. Yu, K. Zhang, Q. Luo, S. Gao, J. Yang and Y. Xie, *Nat. Commun.*, 2022, **13**, 6029.

21 S. Yang, P. Zhang, A. Nia and X. Feng, *Adv. Mater.*, 2020, **32**, 1907857.

22 T. Ban, Y. Kondo and Y. Ohya, *CrystEngComm*, 2016, **18**, 8731–8738.

23 W. Sun, P. Wang, Y. Jiang, Z. Jiang, R. Long, Z. Chen, P. Song, T. Shen, Z. Wu and Y. Xiong, *Adv. Mater.*, 2022, **34**, 2207691.

24 G. Xing, M. Tong, P. Yu, L. Wang, G. Zhang, C. Tian and H. Fu, *Angew. Chem., Int. Ed.*, 2022, **61**, e202211098.

25 Y. Sun, S. Gao and Y. Xie, *Chem. Soc. Rev.*, 2014, **43**, 530–546.

26 M. Cao, C. Hu, Y. Wang, Y. Guo, C. Guo and E. Wang, *Chem. Commun.*, 2003, **15**, 1884–1885.

27 L. Wu, F. Xu, Y. Zhu, A. Brady, J. Huang, J. Durham, E. Dooryhee, A. Marschilok, E. Takeuchi and K. Takeuchi, *ACS Nano*, 2015, **9**, 8430–8439.

28 Z. Ren, R. Zhao, X. Chen, M. Li, X. Li, H. Tian, Z. Zhang and G. Han, *Nat. Commun.*, 2018, **9**, 1638.

29 C. Zhang, Y. Feng, B. Wei, C. Liang, L. Zhou, D. Ivey, P. Wang and W. Wei, *Nano Energy*, 2020, **75**, 104995.

30 K. Zhang, L. Yang, Y. Hu, C. Fan, Y. Zhao, L. Bai, Y. Li, F. Shi, J. Liu and W. Xie, *Angew. Chem., Int. Ed.*, 2020, **59**, 18003–18009.

31 H. Jiang, G. Liu, M. Li, J. Liu, W. Sun, J. Ye and J. Lin, *Appl. Catal., B*, 2015, **163**, 267–276.

32 R. Katal, S. Masudy-Panah, M. Sabbaghan, Z. Hossaini and M. Farahani, *Sep. Purif. Technol.*, 2020, **250**, 117239.

33 C. Zhou, L. Cheng, Y. Li, M. Zeng, Y. Yang, J. Wu and X. Zhao, *Appl. Catal., B*, 2018, **225**, 314–323.

34 D. Ruan, S. Kim, M. Fujitsuka and T. Majima, *Appl. Catal., B*, 2018, **238**, 638–646.

35 W. Zhao, M. Ding, P. Yang, Q. Wang, K. Zhang, X. Zhan, Y. Yu, Q. Luo, S. Gao and Y. Xie, *EES Catal.*, 2023, **1**, 36–44.

36 Z. Wang, L. Zhang, T. Schülli, Y. Bai, S. Monny, A. Du and L. Wang, *Angew. Chem., Int. Ed.*, 2019, **58**, 17604–17609.

37 S. Gao, B. Gu, X. Jiao, Y. Sun, X. Zu, F. Yang, W. Zhu, C. Wang, Z. Feng, B. Ye and Y. Xie, *J. Am. Chem. Soc.*, 2017, **139**, 3438–3445.

38 I. Popescu, N. Tanchoux, D. Tichit and I. Marcu, *Appl. Catal., A*, 2017, **538**, 81–90.

39 A. K. Mishra, A. Roldan and N. Leeuw, *J. Phys. Chem. C*, 2016, **120**, 2198–2214.

40 X. Li, Y. Sun, J. Xu, Y. Shao, J. Wu, X. Xu, Y. Pan, H. Ju, J. Zhu and Y. Xie, *Nat. Energy*, 2019, **4**, 690–699.

41 S. Bai, T. Li, H. Wang, L. Tan, Y. Zhao and Y. Song, *Chem. Eng. J.*, 2021, **419**, 129390.

42 S. Docherty, N. Phongprueksathat, E. Lam, G. Noh, O. Safonova, A. Urakawa and C. Coperet, *JACS Au*, 2021, **1**, 450–458.

43 Y. Liu, H. Zhu, Z. Zhao, N. Huang, P. Liao and X. Chen, *ACS Catal.*, 2022, **12**, 2749–2755.

44 W. Wang, Z. Qu, L. Song and Q. Fu, *J. Energy Chem.*, 2020, **47**, 18–28.